

PREDICTION OF ROTOR-WAKE INTERACTION NOISE USING FINITE-STATE DYNAMIC WAKE INFLOW MODEL

Dhavaleswar Ramaswamy R., Shourav Pednekar, Salini S. Nair, Ranjith Mohan

Department of Aerospace Engineering, Indian Institute of Technology Madras, Chennai, India

Abstract

A good understanding of rotor noise mechanisms, such as blade-vortex, rotor-turbulence and rotor-wake interactions, is essential in order to devise strategies to control them and help in complying with noise regulations. In this paper, the effects of aerodynamic interactions between rotors on acoustics will be investigated. A quick but relatively accurate computation of main rotor-tail rotor as well as coaxial rotors interactions and the resulting unsteady loads that lead to strong acoustic emissions would be useful in developing optimum designs for rotor blades with low noise generating characteristics. The strategy is to utilize finite state wake models to capture the effects of unsteady aerodynamics that are computationally less intensive compared to CFD or free wake methods. The flow-fields above and below the rotor are computed using an extended form of Peters-Morillo model. The Ffowcs Williams-Hawkings equation is used to determine the acoustic field. Acoustic predictions for a coaxial rotor system and for a main rotor-tail rotor configuration with the incorporation of rotor-wake interaction effects are presented. These results are compared with the acoustic signatures obtained for the case of non-interacting rotors. The total noise for the aerodynamically interacting coaxial rotor system is found to be higher by 2-3 dB compared to the aerodynamically non-interacting coaxial rotor system. A similar analysis is done for noise levels of tail rotor which also predicts an increase in SPL by about 2 dB with the inclusion of interaction effects.

1. INTRODUCTION

Noise emissions of rotorcraft vehicles comprise of contribution from aerodynamic and non-aerodynamic sources. The different kinds of aerodynamic noise include impulsive noise due to unsteady flow around blades, broadband noise due to inflow turbulence, etc. Typical helicopter configurations either contain a conventional main rotor-tail rotor system or a coaxial rotor system, which consists of two counter-rotating main rotors. Both rotors of the two systems independently contribute to the generation of near-field and far-field noise. Moreover, in conditions when the wake of one rotor interacts with the other rotor, additional noise is generated, called the rotor-wake interaction noise. For coaxial rotor systems, a significant part of the lower rotor of a coaxial system operates in the wake of the upper rotor, thus, rotor-wake interaction noise is to be always expected. For conventional systems during forward flight, the tail rotor, depending on its relative location, operates in the wake generated by the main rotor.

The aerodynamic environment in both these cases is, therefore, quite complex. The concentrated main rotor tip vortex which falls on the lower rotor or

the tail rotor can generate significant velocity perturbations in the inflow field of that rotor. This results in large unsteady loadings on the rotor blades which contribute to large acoustic pressure fluctuations. Hence, accurately modelling the helicopter rotor wakes is crucial in the prediction of rotor-wake interaction noise. A few attempts have been made to develop prediction methods that estimate rotorcraft noise levels. The Tilt-Rotor Aeroacoustics Code (TRAC) was developed in the 1990s as a rotorcraft noise prediction for tilt-rotors^[1]. In 2005, Boyd et al. presented a comparative study between the acoustic signatures of model rotor and a coaxial system consisting of two counter-rotating rotors using the Comprehensive Analytical Rotorcraft Model for Acoustics (CARMA) system^[1]. The rotor wake was approximated by a system of single tip vortices. The results obtained suggested a significant impact of the interference effects on the noise generating characteristics.

However, on comparisons with experimental results, it was concluded that a vortex filament model for wake representation was not sufficiently accurate for acoustic predictions. Kim et al.^[2] used the Vorticity Transport Model (VTM) to model the aerodynamics of

the rotor systems to study the aeroacoustic characteristics of a coaxial rotor system. But, a more detailed investigation and validation of this wake model is required for predictions of the airloads for acoustics.

The prediction of main rotor wake-tail rotor interaction noise has similarly been impeded due to the difficulty in simulating the mechanisms involved in noise generation. The overall flow field in which the tail rotor operates consists of the main rotor downwash, tip vortices, fuselage wake and turbulence in the flow. The tip vortices are especially strong contributors to loading fluctuations on the tail rotor blades.

This motivates the development of a fast and relatively accurate aeroacoustic analysis tool useful for predicting aerodynamic interactions between the wake and the rotors and the resultant unsteady loads that lead to strong acoustic emissions. A computationally inexpensive tool will also be useful in design and optimization applications where real time simulations are required and CFD solutions are not viable.

In this work, the characteristics of rotor-wake interaction noise are studied. Results are presented for two multiple-rotor configurations – coaxial rotor system and main rotor-tail rotor system. The aerodynamic interaction between the wake and the rotor is modelled using an extension of Peters-Morillo dynamic wake inflow model^[3]. This extended form, developed by Morillo^[4], is used to calculate the velocity fields due to the rotors. The computed airloads and trajectory of the blades form input to the acoustic module, which then computes the noise levels at specified observer locations.

The primary objectives are :

- i. incorporating the effects of unsteady aerodynamics using dynamic inflow model,
- ii. including the unsteady aerodynamic effects of rotor wake interactions on acoustics,
- iii. predicting the noise of rotors which lie in the wake of or interact with other aerodynamic surfaces such as in the case of coaxial rotors and main rotor-tail rotor combination.

2. DYNAMIC WAKE INFLOW MODELLING

The rotor-wake interaction noise is sensitive to the accurate modeling of the transient blade surface pressure fluctuations in the interaction process. The aerodynamic characteristics of rotor-wake interactions, however, are complex in nature and have not been widely studied for either main rotor-tail rotor systems or coaxial rotor systems. In order to address this

problem, a suitable model for computation of induced velocities by the rotor is required. The unsteady effects for these configurations are captured by using an extension of the Morillo model^[4,5], which is a finite-state dynamic wake inflow model. This model, which is based on the Peters-He dynamic wake model^[3], allows for the computation of induced velocities throughout the flow-field. This gives us a scope to study the interaction of two rotor systems, and predict the rotor-wake interaction noise using velocities induced in the wake below the rotor^[6].

In this work, the Morillo model^[4] is used for computing velocities above the rotor plane (potential regime). In this model, the equations that define the flow are re-derived from first principles to compute the whole flow field with all of the components for the volume above the rotor disk. The model uses continuity and momentum equations in three dimensions around the actuator disk to capture the flow. Zhongyang Fei^[6] extended Morillo's model^[4] and developed an equation for the flow below the plane of the rotor (rotational regime), which allows application of finite-state methods within the rotor wake giving the entire velocity field at all points – above and below the rotor plane. The basic governing equations are:

$$\nabla \cdot \vec{V} = 0$$

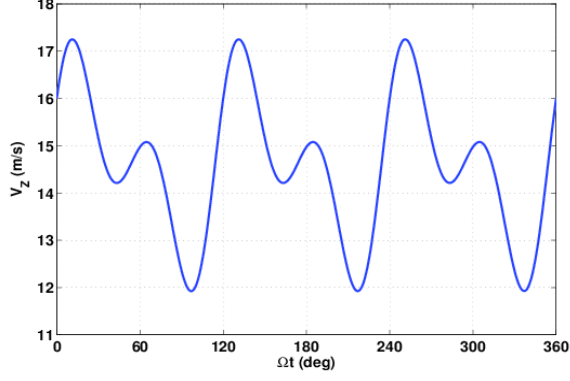
$$\frac{\partial \vec{V}}{\partial t} - V_{\infty} \frac{\partial \vec{V}}{\partial \xi} = \frac{-\Delta P}{\rho}$$

where V_{∞} is the free stream velocity.

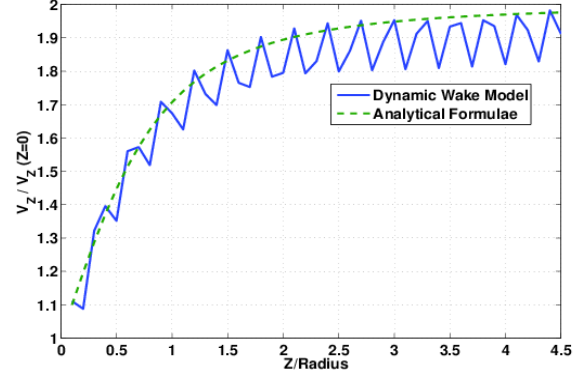
Pressure and velocity potentials are introduced as $P/\rho = \Phi$ and $\vec{V} = \nabla \Psi$, and the Cartesian system (x, y, z) is converted to ellipsoidal coordinate system (v, η, ψ) which captures pressure discontinuities across the rotor disk. Both pressure and velocity potentials satisfy Laplace's condition i.e. $\nabla^2 \Phi = 0$ and $\nabla^2 \Psi = 0$. The potentials are expressed as $\Phi(v, \eta, \psi) = \Phi_1(v) \Phi_2(\eta) \Phi_3(\psi)$ where Φ_1 and Φ_2 are expressed using Legendre polynomials of first and second kind respectively and Φ_3 using Fourier series. Velocity potential is similarly expressed. The final velocity and pressure terms are expressed as below:

$$\frac{P}{\rho} = - \sum_{m=0}^{\infty} \sum_{n=m+1}^{\infty} \left(\tau_n^{mc} \Phi_n^{mc} + \tau_n^{ms} \Phi_n^{ms} \right)$$

$$\vec{V} = \sum_{m=0}^{\infty} \sum_{n=m+1}^{\infty} \left(a_n^{mc} \Psi_n^{mc} + b_n^{ms} \Psi_n^{ms} \right)$$



(a) v_z vs t at one rotor radius below the rotor disk.



(b) v_z vs z at an instantaneous time

Figure 1: Time and spatial variation of inflow velocity v_z for a three bladed rotor at $r/R = 0.5$, $\psi = 0$. See Ref. [7] for analytical formula used in (b).

where,

$$\Phi_n^{mc} = P(v)Q(i\eta)\cos(m\psi) \quad , \quad \Psi_n^{mc} = \sigma_n^m \Phi_{n+1}^m + \zeta_{n+1}^m \Phi_{n-1}^m \quad ,$$

a_n^m, b_n^m are cosine, and sine induced inflow expansion coefficients, τ_n^{mc}, τ_n^{ms} are cosine and sine parts of pressure potentials, Φ_n^{mc}, Φ_n^{ms} are cosine and sine potentials, Ψ_n^{mc}, Ψ_n^{ms} are cosine and sine parts of velocity potentials, m is the harmonic number, n is the polynomial number. The Galerkin approach is used to transform the momentum conservation equation to a set of ordinary differential equations which is then solved. The cosine and sine functions completely separate into two uncoupled sets during this procedure (see Ref. [4]), giving the time evolution of coefficients as:

$$[M^c][a_n^{mc}] + [D^c]V_\infty[\tilde{L}^c]^{-1}[M^c][a_n^{mc}] = [D^c][\tau_n^{mc}]$$

$$[M^s][b_n^{ms}] + [D^s]V_\infty[\tilde{L}^s]^{-1}[M^s][b_n^{ms}] = [D^s][\tau_n^{ms}]$$

where $[M]$ is mass matrix, $[D]$ is damping matrix, $[\tilde{L}]$ is influence coefficient matrix. Here τ_n^m is coefficient of pressure potential, and is related to thrust calculated by Blade Element Momentum (BEM) theory as:

$$\tau_n^{0c} = \frac{1}{2\pi\rho R} \sum_{q=1}^Q \int_0^1 L_q(r,t)\Phi_n^{0c}(v)dr$$

$$\tau_n^{mc} = \frac{1}{\pi\rho R} \sum_{q=1}^Q \int_0^1 L_q(r,t)\Phi_n^{mc}(v)\cos(m\psi)dr$$

$$\tau_n^{ms} = \frac{1}{\pi\rho R} \sum_{q=1}^Q \int_0^1 L_q(r,t)\Phi_n^{ms}(v)\sin(m\psi)dr$$

L_q is blade cross section lift.

The Zhongyang Fei model^[6] is used for the velocity field below the rotor plane. The velocity at any point in the wake $(r_o, \psi_o, \varepsilon_o)$ is defined as the sum of velocity at a point on the disk and two adjoint velocities at centro-symmetric points $(r_o, \tilde{\psi}_o, 0)$ and $(r_o, \tilde{\psi}_o, -\varepsilon_o)$ (see Ref. [6]).

$$\vec{V}(r_o, \psi_o, \varepsilon_o, \tau) = \vec{V}(r_o, \psi_o, 0, \tau - \tau_{\varepsilon_o}) + \vec{V}_{adj}(r_o, \tilde{\psi}_o, 0, \tau - \tau_{\varepsilon_o}) - \vec{V}_{adj}(r_o, \tilde{\psi}_o, -\varepsilon_o, \tau)$$

The adjoint velocity, \vec{V}_{adj} , is defined as,

$$\vec{V}_{adj}(r_o, \psi_o, \varepsilon_o, \tau) = \sum_{m=0}^{\infty} \sum_{n=m+1}^{\infty} (\Delta_n^{mc} \Psi_n^{mc} + \Delta_n^{ms} \Psi_n^{ms})$$

where Δ_n^m is the adjoint velocity expansion coefficient. And the governing equation of adjoint states is given by:

$$-[M^c][\Delta_n^{mc}] + [D^c]V_\infty[M^c][\Delta_n^{mc}] = [D^c][K^c][\tau_n^{mc}]$$

$$\text{where } [K^c] = \begin{bmatrix} \ddots & & & & \\ & \ddots & & & \\ & & (-1)^{n+1} & & \\ & & & \ddots & \\ & & & & \ddots \end{bmatrix}$$

Figure 1(a) shows the time variation of axial velocity, v_z , at a point within the wake, one rotor radius below the rotor disk. Figure 1(b) shows the instantaneous value of v_z at different points below the rotor.

3. ACOUSTIC PREDICTION METHOD

The acoustic field of the helicopter rotor is computed using the Ffowcs Williams-Hawkings (FW-H) equation^[8]:

$$(1) \quad \left[\frac{1}{c^2} \left(\frac{\partial^2}{\partial t^2} \right) - \nabla^2 \right] p'(\mathbf{x}, t) = \frac{\partial}{\partial t} [(\rho_o v_n) \delta(f)] - \frac{\partial}{\partial x_i} [(\Delta P_{ij} n_j) \delta(f)] - \frac{\partial^2}{\partial x_i x_j} [T_{ij} H(f)]$$

where $f=0$ represents the source (blade) surface, c is the speed of sound, p' is the acoustic pressure and ρ_o is the fluid density in quiescent medium, v_n is local normal velocity of source surface, P_{ij} is the compressive stress tensor, \mathbf{n} is the unit outward normal vector to surface, with components, n_j , T_{ij} is the Lighthill stress tensor, \mathbf{x} is the observer position vector, t is the observer time, $\delta(f)$ is the Dirac delta function and $H(f)$ is the Heaviside function.

The FW-H equation^[8] is an extension of Lighthill's acoustic analogy^[9] which is an exact governing equation of noise generation away from the flow region. The generalization of Lighthill's equation in the presence of moving surfaces is the FW-H equation. The FW-H equation has been in use for the prediction of aerodynamically generated noise of rotating blades such as high speed propellers and helicopter rotors. Eq. 1 relates two domains, one describing the generation of sound, the other describing its propagation. The monopole and dipole sources (first two terms on the right hand side of Eq. 1) are the surface source terms while the quadrupole source (third term on the right hand side of Eq. 1) is a volume source term. The monopole and dipole surface source terms of the FW-H equation account for the thickness and loading noise respectively; quadrupole source term includes turbulent noise. The thickness (monopole) source term models the noise generated by the displacement of fluid as the blade passes in the flow medium. The loading (dipole) source term models the noise that results from the unsteady force distribution on the blade surface. The quadrupole source term includes the effects of complex noise sources inside a fluid volume surrounding the rotor blades capturing noise due to turbulence and transonic flow field. Noise due to quadrupole terms is neglected in the present work as it is significant only for high speed flows^[10].

The blade surface is considered to be constituted of several panels acting as sources of

sound. The noise produced by these sources is then propagated according to Eq. 1. The acoustic noise estimation follows Formulation 1A^[10], which is an integral formulation of the FW-H equation. Developed by Brentner and Farassat^[10,11], Formulation 1A does a retarded time integration of the governing equation. Acoustic pressure can, thus, be obtained in terms of surface integrals of the surface pressures and velocities and their normal and time derivatives. The instantaneous acoustic pressure at a given observer location given by,

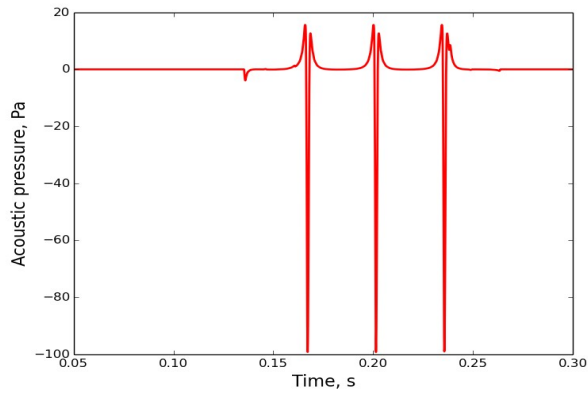
$$p'(\mathbf{x}, t) = p'_T(\mathbf{x}, t) + p'_L(\mathbf{x}, t) \quad \text{where,}$$

$$4\pi p'_T(\mathbf{x}, t) = \int_{f=0} \left[\frac{\rho_o (v_n + v_n)}{r |1 - M_r|^2} \right]_{ret} dS + \int_{f=0} \left[\frac{\rho_o v_n (r \dot{M}_r + c M_r - c M^2)}{r^2 |1 - M_r|^3} \right]_{ret} dS$$

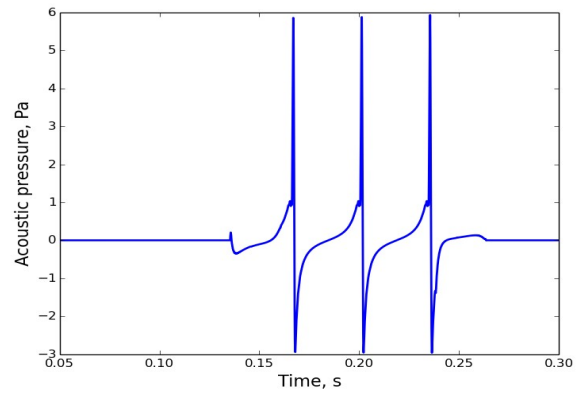
$$4\pi p'_L(\mathbf{x}, t) = \frac{1}{c} \int_{f=0} \left[\frac{\dot{l}_r}{r |1 - M_r|^2} \right]_{ret} dS + \int_{f=0} \left[\frac{l_r - l_M}{r^2 |1 - M_r|^2} \right]_{ret} dS + \frac{1}{c} \int_{f=0} \left[\frac{l_r (r \dot{M}_r + c M_r - c M^2)}{r^2 |1 - M_r|^3} \right]_{ret} dS$$

Here subscripts T and L denote thickness and loading noise components respectively, \mathbf{M} is the surface velocity vector normalized by c , $M = |\mathbf{M}|$, $l_i = \Delta P_{ij} n_j$ is the local force intensity acting on the fluid, dS is an element of the rotor blade surface, \mathbf{r} is the unit radiation vector, r is the distance between the observer and the source. Dot over a variable implies the source time derivative of that variable and the subscripts n, r and M refer to dot product with \mathbf{n}, \mathbf{r} and \mathbf{M} vectors respectively. The subscript ret implies that the integrand is evaluated at the retarded time when the source emits sound.

Preliminary results of acoustic noise prediction for an isolated rotor by incorporating the finite-state wake model are presented. A code based on Formulation 1A and source-time dominant algorithm is developed to compute the noise levels at any arbitrary location with respect to the helicopter rotor. In the source-time dominant algorithm, the terms in square bracket are evaluated at the source (retarded) time rather than the observer time. That is, the time when a panel generates sound is chosen and the time taken by the signal to reach the observer is determined. This panel time history can be interpolated to provide the contribution at the desired observer times.



(a) Thickness noise



(b) Loading noise

Figure 2: Time history of predicted noise over one rotor revolution at an observer location 10^*R distance away from rotor center.

The results, as shown in Figures 2 to 4, correspond to a three-bladed single rotor system with NACA 0015 airfoil sections. The rotor diameter is 10 m and the blade chord is 0.4 m. The tip Mach number is kept at 0.9 in order to compare with results presented in Ref. [12].

Figure 2 shows the acoustic signatures for an observer in the plane of the rotor, 50 m (10^*R) away from the center of rotation. Sound Pressure Levels (SPL) of the maximum acoustic pressure at several points in the plane of the rotor (disk) and equidistant from rotor center (sphere) have been plotted in Figures 3 and 4. The figures indicate directionality of the predicted noise in addition to its maximum amplitude. Figure 3 shows the SPL distributions for the case when only collective ($\theta_0=5^\circ$) control is applied. From Figure 3, the axisymmetry of maximum thickness and maximum loading noise signals can be observed. As noted by researchers in the past [3,8], maximum radiation of the thickness noise signal occurs in the plane of rotation and there is reduction in the amplitude at higher elevation, both of which can be seen from Figure 3(a). The loading noise signal in Figure 3(b) shows two bands of high amplitude approximately equidistant from the central plane of rotation. The intensity of the noise signal is higher for the lower band as indicated by the color map. The maximum directivity of this signal occurs 19° below the plane of rotation which agrees reasonably well with results in Ref. [13].

The SPL distribution on the spherical surface for the case of the rotor system with cyclic control inputs ($\theta_c=3^\circ, \theta_s=0^\circ$) are shown in Figures 4(a) and 4(b). As expected, the maximum thickness

noise is still axisymmetric, but the maximum loading noise signal shows azimuthal variation. This is observed clearly in Figure 4(d).

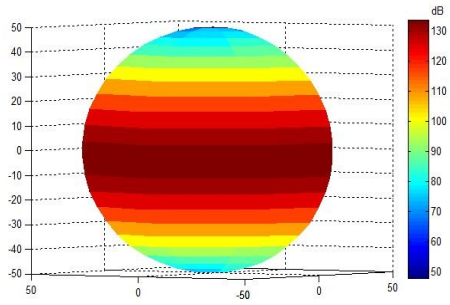
Thus, unsteady aerodynamic effects are included using finite-state dynamic inflow model and utilized for acoustic predictions. The present work aims to predict the aerodynamically generated noise due to these surface source terms for multi-rotor helicopter configurations such as a conventional main rotor-tail rotor system and a coaxial rotor system.

4. RESULTS

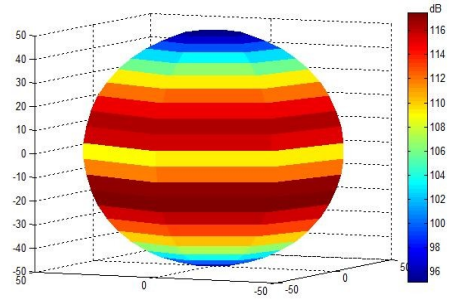
4.1 Model Geometry

The coaxial rotor configuration used in this study is constructed using two identical three-bladed rotors, separated vertically by 20% of the rotor radius. The rotor blades are rectangular, untwisted and have NACA0012 airfoil sections along the span. The rotor diameter is 10 m and the blade chord is 0.4 m. The hover tip Mach number is 0.62. The phase angle is set to zero, that is, the blades of the upper and lower rotors are aligned at zero azimuth which lies along the direction of free-stream. The lower rotor rotates counter-clockwise while the upper rotor rotates clockwise.

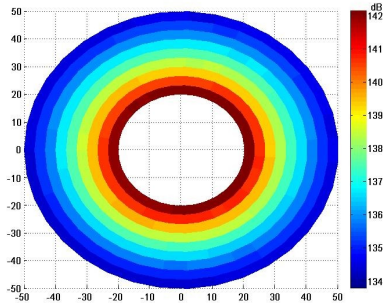
For the main rotor-tail rotor configuration, the main rotor geometry is identical to the geometry of rotors used in the case of coaxial system. The distance between the hub of the main rotor and the tail rotor center is 1.5^*R ($R = 5$ m) along horizontal axis. The tail rotor center is located 0.2^*R below the main rotor plane. Sections of the two-bladed tail rotor are modelled with NACA0012 airfoil and the pitch angle is



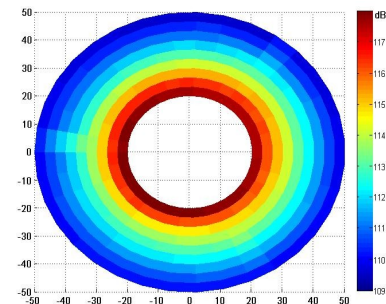
(a) Thickness noise on spherical surface



(b) Loading noise on spherical surface

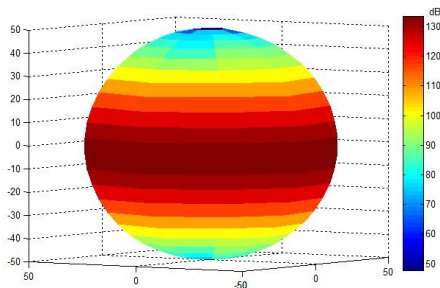


(c) Thickness noise in rotor plane

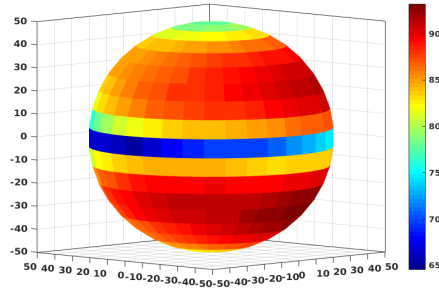


(d) Loading noise in rotor plane

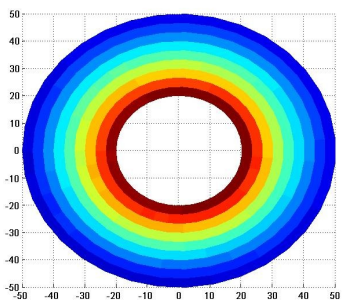
Figure 3: SPL in dB for an isolated rotor with collective input



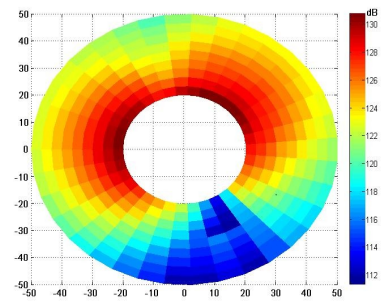
(a) Thickness noise on spherical surface



(b) Loading noise on spherical surface



(c) Thickness noise in rotor plane



(d) Loading noise in rotor plane

Figure 4: SPL in dB for an isolated rotor with cyclic input

5° without twist angle. The radius of tail rotor is 1 m, and the aspect ratio of tail rotor blade is 2.5.

4.2 Coaxial Rotor System

Predictions of the rotor inflow velocities and noise levels are shown for two cases - aerodynamically non-interacting and aerodynamically interacting rotors. Both cases are trimmed separately. The rotor collective and cyclic pitch controls are adjusted to achieve equal thrust. The analysis of the inflow and acoustic characteristics of the coaxial rotors are presented for two representative flight operating conditions (hover and forward flight) in order to highlight the differences in the acoustic response of the system when only collective input is applied (in hover) and when both collective and cyclic inputs are applied (in forward flight).

For the case of non-interacting rotors, the wake interference effects have been artificially switched off. Thus, the upper and lower rotors are in aerodynamic isolation. Figure 5 shows the instantaneous inflow velocity fields over the rotor disk for this case. The velocity fields are identical for upper and lower rotors. The inflow for hover is shown in Figure 5(a). The inflow velocities are seen to peak at regions present around the blade tip locations at given time instant. The symmetry of the inflow for hover can be observed. The symmetry is not present in the inflow for forward flight due to cyclic control inputs as shown in Figure 5(b). The velocity magnitudes for forward flight are also lower than those observed for hover. Aerodynamically, however, the two rotors of the coaxial system will interact based on their relative distance. The interaction between the rotors is modelled as follows:

$$(2) \quad \vec{V}_{R1} = \vec{V}_{11} + \vec{V}_{12}$$

$$(3) \quad \vec{V}_{R2} = \vec{V}_{21} + \vec{V}_{22}$$

where \vec{V}_{R1} is total induced velocity on the upper rotor, \vec{V}_{R2} is total induced velocity on the lower rotor.

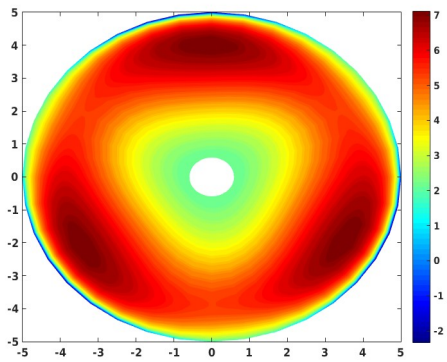
\vec{V}_{ij} is velocity induced on rotor 'i' by potential of rotor of 'j'. For calculation of \vec{V}_{11} , \vec{V}_{12} , \vec{V}_{22} , the Morillo model is sufficient, but for \vec{V}_{21} , the Zhongyang Fei model is used.

Since these two rotors are interacting, the thrust on each rotor may not be the same. But the control inputs are applied such that the total thrust for the interacting rotors case equals the total thrust for the independent, non-interacting rotors. Figures 6 and 7 show that both the rotors induce additional inflow velocities on the other rotor. In addition, it can be seen that the upper rotor induces a larger additional vertical

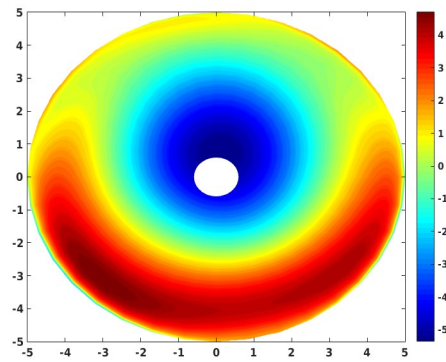
inflow component on the lower rotor than what the lower rotor induces on the upper rotor. This is true for both hover and forward flight. The additional induced velocities are significantly larger for the two rotors in hover than in forward flight. The inflow field, though, still remains symmetric for hover condition and asymmetric for forward flight as in the case for non-interacting rotors.

Figures 8, 9, 10 and 11 show plots of the maximum sound pressure level (SPL) over one rotor revolution that is produced on a horizontal observer plane located in the plane of the lower rotor. The predicted noise plots for the non-interacting coaxial rotors in hover condition are axisymmetric as shown in Figure 8. Results of the acoustic analysis for interacting rotors are presented next. Here, the aerodynamics on one rotor is influenced by the induced inflow velocities from the other rotor. Thus, due to these mutual interactions, the blade motions and airloads of each rotor will be different. Hence, both thickness and loading noise will be affected by the inclusion of wake interaction. Like the SPL plots for the case of non-interacting coaxial rotors, the predicted noise level plots for aerodynamically interacting coaxial rotors are also axisymmetric, as shown in Figure 9. The SPL increases for both upper and lower rotors when rotor-wake interference effects are included. The resulting SPL is about 2-3 dB higher in comparison with the respective SPL of non-interacting rotors. Thus, there is clear indication of the rotor-wake interaction noise. Also, the noise levels of the upper rotor are more than that of the lower rotor. This could be because the observer is in the plane of the lower rotor and the loading noise contribution from the upper rotor is higher out of the rotor plane, directed at an angle below the source.

Similar results were also produced for the forward flight condition as shown in Figures 10 and 11. The skew angle was set to 5° with a low advance ratio of 0.04 (approximately climb case). Comparing results from non-interacting rotors and interacting rotors, Figures 10(a) and 11(a) show that there is only a small change in magnitude of SPL as well as directivity for the upper rotor in the two cases. However, for the lower rotor, a considerable difference in the SPL distribution for interacting and non-interacting rotors can be seen from Figures 10(b) and 11(b). Figure 11(b) shows that maximum acoustic pressures of higher magnitudes are distributed in a larger space over the concerned observer plane. This could be attributed to higher additional induced velocities on the lower rotor due to the impingement of wake velocities of the upper rotor compared to the additional induced velocities on upper rotor.

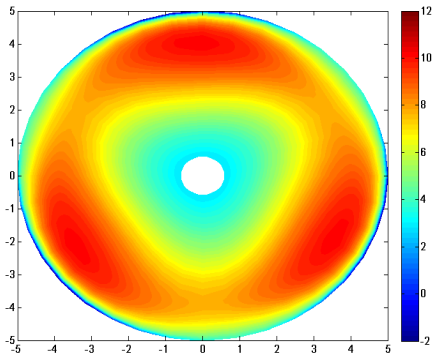


(a) Hover

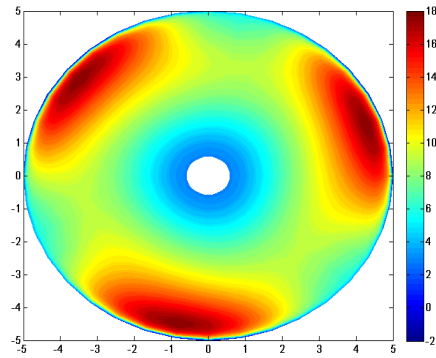


(b) Forward flight

Figure 5: Inflow velocities in m/s of the aerodynamically non-interacting coaxial rotor system.

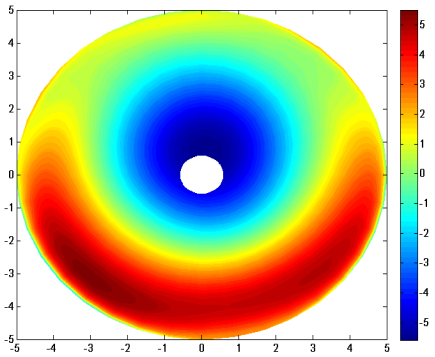


(a) Upper Rotor

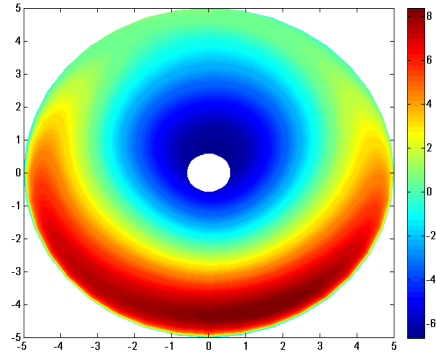


(b) Lower Rotor

Figure 6: Inflow velocities in m/s of the aerodynamically interacting coaxial rotor system in hover.

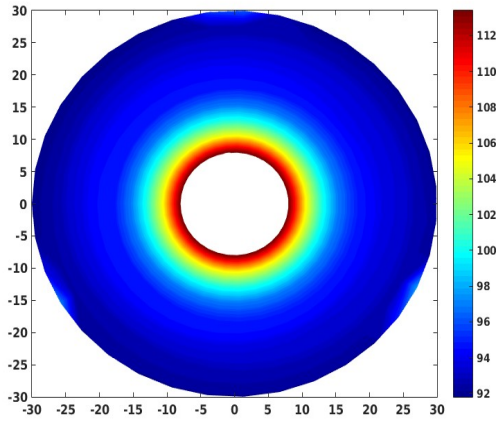


(a) Upper Rotor

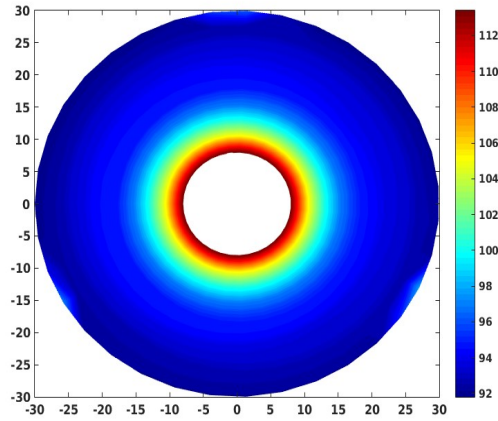


(b) Lower Rotor

Figure 7: Inflow velocities in m/s of the aerodynamically interacting coaxial rotor system in forward flight.

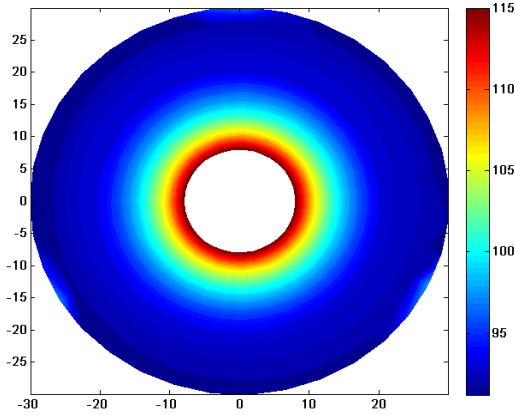


(a) Upper Rotor

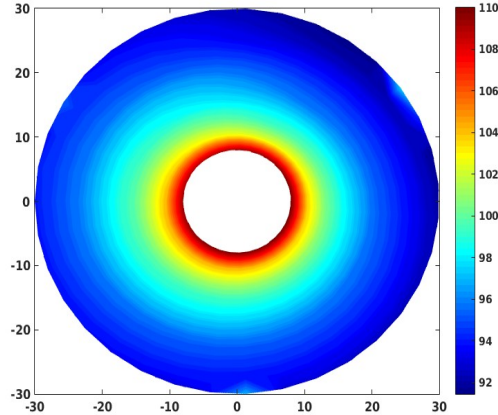


(b) Lower Rotor

Figure 8: Predicted noise levels in dB of the aerodynamically non-interacting coaxial rotor system in hover.



(a) Upper Rotor



(b) Lower Rotor

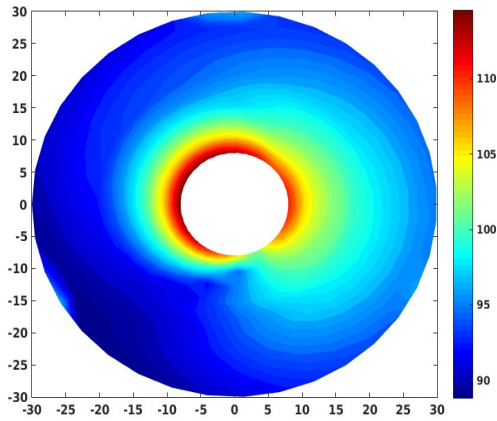
Figure 9: Predicted noise levels in dB of the aerodynamically interacting coaxial rotor system in hover.

4.3. Main rotor-tail rotor system

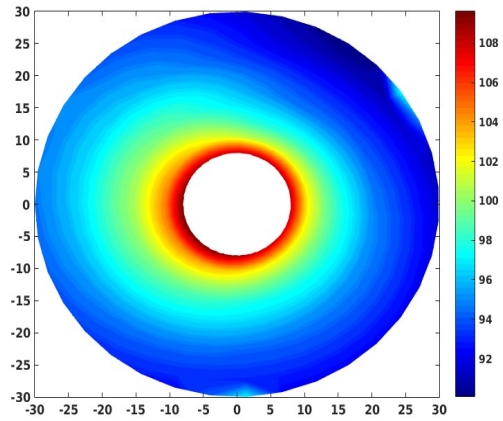
Here, it is assumed that the presence of the tail rotor has no effect on the main rotor wake generation, and no fuselage wake effect is included. Modelling of the interaction between the main rotor and tail rotor follows Eq. 2 and Eq. 3. In this case, '1' corresponds to main rotor, and '2' to tail rotor. The effect of tail rotor on main rotor is neglected i.e. $\vec{V}_{12} \approx 0$. The axes are different for main rotor and tail rotor. Hence, \vec{V}_{R1} and \vec{V}_{R2} have different coordinate systems.

Predictions of the in-plane velocities and noise levels are shown. The two cases – no interference and interference - are trimmed individually to achieve equal tail rotor thrust. A disk angle of attack of 7° corresponding to wake skew angle of 83° is assumed. The forward speed is 10 m/s.

The velocities in the wake of the main rotor have all three components. The dominant component of these wake velocities lie in the plane of the tail rotor. The in-plane velocities include radial and azimuthal components, V_r and V_ψ respectively. The azimuthal component affects the generation of both thickness and loading noise. Figure 12 shows the

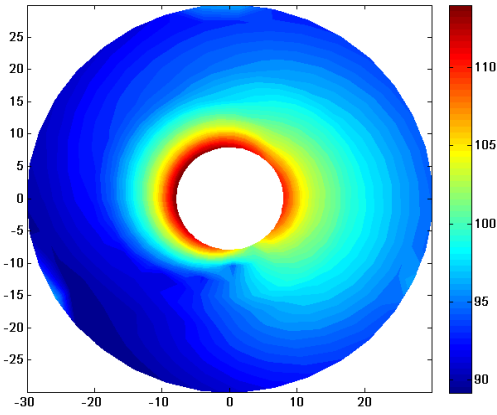


(a) Upper Rotor

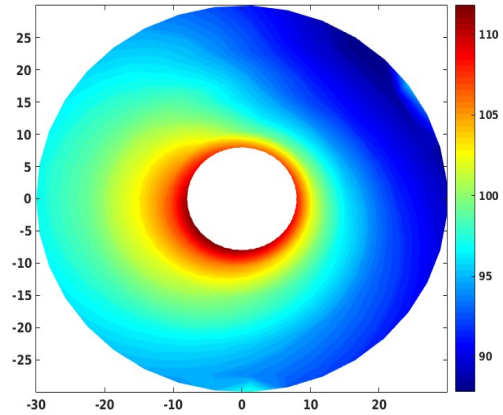


(b) Lower Rotor

Figure 10: Predicted noise levels in dB of the aerodynamically non-interacting coaxial rotor system in forward flight.



(a) Upper Rotor



(b) Lower Rotor

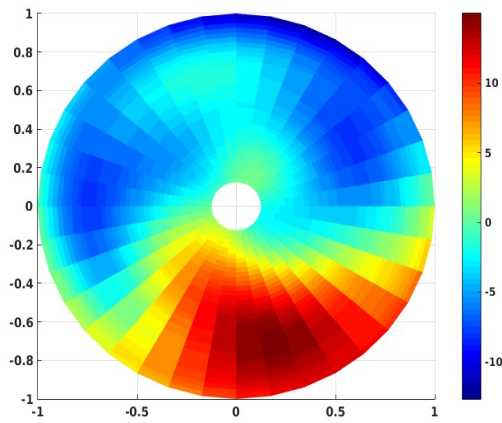
Figure 11: Predicted noise levels in dB of the aerodynamically interacting coaxial rotor system in forward flight.

variation of azimuthal component of in-plane velocities, V_{ψ} , (excluding rotational speed) with and without main rotor wake interaction.

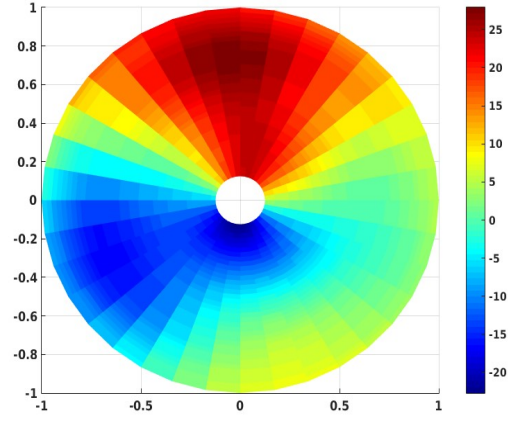
Figure 13 shows the SPL distribution over a disk in the tail rotor plane. Comparison of the results obtained for non-interference case and interference case suggests that on inclusion of main rotor wake-tail rotor interaction effects, SPL is about 2 dB higher. Figure 14 shows the total tail rotor noise signatures at a point 2^*R away from the tail rotor center. The difference in the maximum amplitudes can be observed from the plots in Figures 14(a) and 14(b).

5. CONCLUSIONS

A computationally less expensive way of predicting rotor-wake interaction noise for multi-rotor configurations has been demonstrated. The interaction noise has been analyzed using a finite-state dynamic wake inflow model with the acoustic code based on the Ffowcs Williams-Hawkings formulation. The ability of the dynamic wake model to predict inflow velocities above and below the rotor allows the modelling of unsteadiness due to rotor-wake interactions. It is important to note that the finite-state dynamic wake inflow model is not a replacement to predict inflow

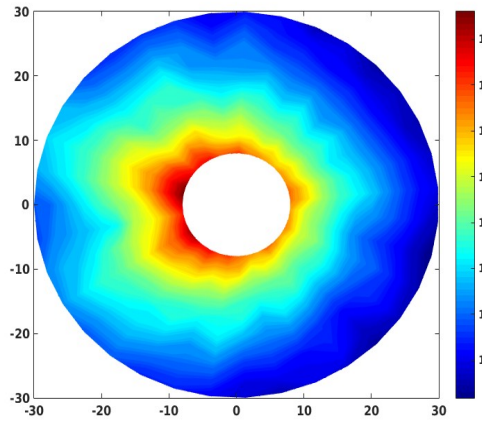


(a) No interference

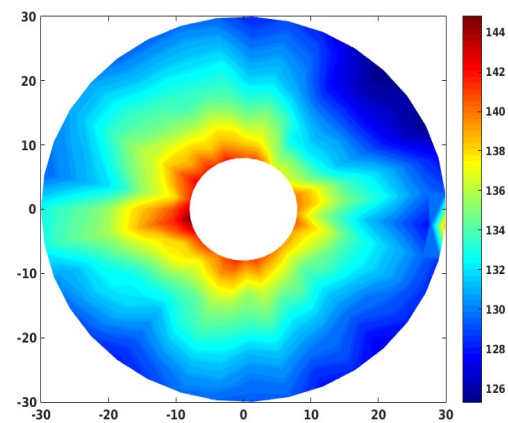


(b) With interference

Figure 12: Azimuthal component of in-plane velocities in m/s experienced by the tail rotor in forward flight.

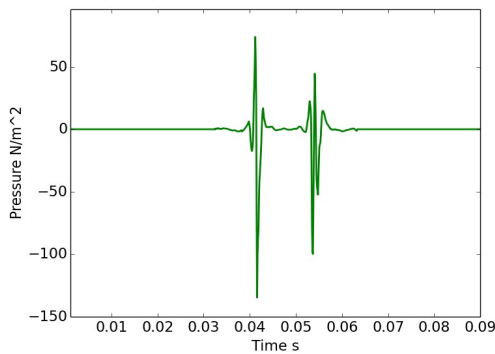


(a) No interference

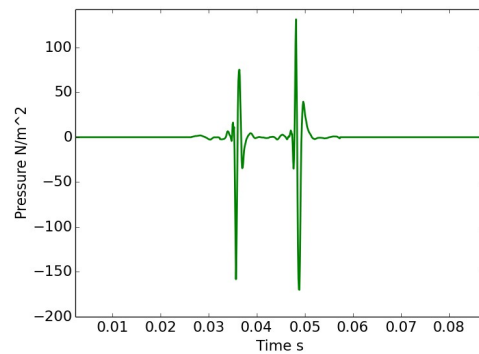


(b) With interference

Figure 13: Predicted noise levels in dB of tail rotor in forward flight with and without main rotor wake interaction.



(a) No interference



(b) With interference

Figure 14: Predicted time history of acoustic pressure at a point in the tail rotor plane 10 m away from the center along the direction opposite to the free stream axis.

velocities accurately, but only a reasonably good tool to compute the unsteady component in the flow. To illustrate the interaction and acoustic prediction capability, two multi-rotor configurations were examined. Noise due to rotor-wake interaction was highlighted by contrasting with acoustic results obtained on neglecting wake interference effects. Examining the induced inflow velocities and SPL noise plots for each rotor in aerodynamically non-interacting coaxial rotor system and aerodynamically interacting coaxial rotors, it appears that the aerodynamic and acoustic effects of rotor interference are significant. A similar acoustic analysis is done for a conventional helicopter configuration with a main rotor and a tail rotor. For both the coaxial rotor system and main rotor-tail rotor system, the SPL on inclusion of interaction effects is found to be 2-3 dB higher compared to the no interference cases. Though this is not a complete study, the acoustic differences show that it is important to account for mutual aerodynamic interactions between the rotors.

COPYRIGHT STATEMENT

The authors confirm that they, and/or their company or organization, hold copyright on all of the original material included in this paper. The authors also confirm that they have obtained permission, from the copyright holder of any third party material included in this paper, to publish it as part of their paper. The authors confirm that they give permission, or have obtained permission from the copyright holder of this paper, for the publication and distribution of this paper as part of the ERF proceedings or as individual offprints from the proceedings and for inclusion in a freely accessible web- based repository.

REFERENCES

[1] Boyd Jr. DD, Burley CL and Conner DA. Acoustic Predictions of Manned and Unmanned Rotorcraft Using the Comprehensive Analytical Rotorcraft Model for Acoustics (CARMA) Code System. *American Helicopter Society International Specialists' Meeting on Unmanned Rotorcraft*. Phoenix, AZ, 18–20 January 2005.

[2] Kim HW, Duraisamy K and Brown R. Aeroacoustics of a Coaxial Rotor in Level Flight. *American Helicopter Society 64th Annual Forum*. Montreal, April 29 - May 1, 2008.

[3] Peters DA, Boyd DD and He CJ. A Finite-State Induced-Flow Model for Rotors in Hover and Forward Flight. *Journal of the American Helicopter Society*, Vol. 34, No. 4, pp 5-17, 1989.

[4] Morillo JA. A Fully Three-Dimensional Unsteady Rotor Inflow Model Developed in Closed Form from a Galerkin Approach (2001). *Doctor of Science Dissertation*. Washington University, 2001.

[5] Garcia-Duffy C. Applying Dynamic Wake Models to Induced Power Calculations for an Optimum Rotor. *Doctor of Science Dissertation*. Washington University, 2008.

[6] Fei Zhongyang. A rigorous solution for finite state inflow through the flow field. *Doctor of Philosophy Dissertation*. Washington University, 2013.

[7] Leishman JG. *Principles of helicopter aerodynamics*. Cambridge University Press, 2002.

[8] Ffowcs Williams JE and Hawking DL. Sound generated by turbulence and surfaces in arbitrary motion. *Philosophical Transactions of the Royal Society*, Vol. A264, Issues 1151, pp 321-342, 1969.

[9] Lighthill MJ. On Sound Generated Aerodynamically. I: General Theory. *Proc R Soc A*, Vol. 211, Issues 1107, pp 564-587, 1952.

[10] Brentner KS and Farassat F. Modeling Aerodynamically Generated Sound for Helicopter Rotors. *Progress in Aerospace Sciences*, Vol. 39, Issues 2-3, pp 83-120, 2003.

[11] Brentner KS and Farassat F. The uses and abuses of the acoustic analogy in helicopter rotor noise prediction. *AHS Specialists' Meeting on Aerodynamics and Aeroacoustics, Arlington, Texas*. American Helicopter Society International, Inc., 1987.

[12] Farassat F. Theory of Noise Generation from Moving Bodies with an Application to Helicopter Rotors. *NASA Technical Report*, NASA TR R-451, 1975.

[13] Conner DA. Measurement resolution of Noise Directivity Patterns from Acoustic Flight Tests. *NASA Technical Report*, NASA TR 89-B-004, 1989.